Acta Astronautica 233 (2025) 302–314

Contents lists available at ScienceDirect

Acta Astronautica

journal homepage: www.elsevier.com/locate/actaastro

Unexplained starlight pulses found in optical SETI searches

Richard H. Stanton

Jet Propulsion Laboratory (retired), Shay Meadow Observatory, Big Bear City, CA, 92314, USA

ARTICLE INFO

Keywords:
Fast pulse pairs in starlight
Optical SETI
Bipolar optical pulses
Fast star photometry

ABSTRACT

Years spent searching more than 1300 sun-like stars for optical SETI signals have finally yielded unexpected results. A "signal" of two fast identical pulses, separated by 4.4s, was discovered in the light of HD89389. No single pulses, even remotely resembling these, have been found in these searches. Close examination of this signal reveals that several unique features of the first pulse are repeated almost exactly in the second. Comparison of this signal with those of airplanes, satellites, meteors, lightning, atmospheric scintillation and system noise, emphasizes their uniqueness. During the re-examination of historical data, another pair of similar pulses was found in an observation of HD217014 made four years earlier. Not fully explained at the time, this signal had been dismissed simply as "birds." After all pulses were examined in detail, and shown that they could not have been made by birds, several theories are proposed that might explain their origin. A theory based on edge diffraction is discussed in some detail. If correct, this theory should enable future observations to measure the distance to the occulting object, and using arrays of telescopes, determine its size, shape and velocity.

1. Introduction

A 30-inch telescope located in Big Bear, California, has been used over the last several years to search for optical SETI signals in the light of nearby, sun-like stars [1,2]. An hour of high-speed photometry is recorded during each observation. These data are searched in both the time and frequency domains for any signals that might be present in the star's light, possibly added by extraterrestrials. The only clear, unambiguous signals found to date have been the two pairs of strange pulses described here. Several features of these pulses are unique, supporting their characterization as "strange." In each pulse the star's light increases, decreases and then increases again in a fraction of a second. The rapidity of these changes proves that whatever is causing them cannot be as far away as the stars themselves. This fact leaves the door open to a variety of possible explanations, perhaps lowering the chance that any extraterrestrial intelligence is involved.

The approach used here is different from that employed in many other optical SETI searches. Some [3,4] look for nanosecond pulses of sufficient intensity to momentarily outshine the host star's light, as first suggested by Schwartz and Townes [5]. Others search optical spectra of stars for unusual features [6] or emission close to a star that could have been sent from an orbiting planet [7]. The equipment used here is not capable of making any of these measurements. Instead it relies on detecting unexplained changes in a star's light as indications of intelligent activity. Starting with time samples of 100μs, the search is capable of detecting optical pulses of this duration and longer, and also of finding optical tones in the frequency range ~0.01–5000Hz.

An overview of the observation program, including photometer design and the automated search program used to find hidden signals, is provided in Section 2. Typical data products are shown in this overview, including examples of common sources of very fast signals, such as airplanes, satellites and meteors. Photometry of both pairs of strange pulses is shown in Section 3, including a summary of what makes them unique. Several ideas of how these pulses might be generated are listed in Section 4. While no final choice is made, the theory that these pulses result from edge diffraction by a distant object seems to have merit, and is discussed in more detail in Section 5. Finally, a path for future work is suggested in Section 6 that includes a plea for constructing arrays of optical telescopes that could greatly improved our understanding of any future events.

2. Observation program

2.1. Instrumentation

2.1.1. Photometer

A schematic of the photometer is shown in Fig. 1. The purpose of this instrument is to look for variations in starlight that might be attributed to extraterrestrial intelligence. As such, the emphasis is on measuring changes in intensity over as wide a frequency range as possible. Light from each target star is measured using three separate PMTs at the prime

E-mail address: rhstanton@gmail.com.

https://doi.org/10.1016/j.actaastro.2025.04.044
Received 9 November 2024; Received in revised form 5 April 2025; Accepted 22 April 2025
Available online 23 April 2025

Acronyms/abbreviations

ETI	Extraterrestrial Intelligence
FFT	Fast Fourier Transform
GLD	Geometric Light Disk
GEO	Geosynchronous Earth Orbit
IOTA	International Occultation Timing Association
OTA	Optical Telescope Array
PMT	Photomultiplier Tube (generating photon pulses)
SETI	Search for Extraterrestrial Intelligence

focus of a 30″ f/3.9 telescope. A fourth channel monitors the background light in the ~5arcmin diameter annulus immediately surrounding the 41arcsec diameter star diaphragm. The channels have different spectral band-passes: CLR and BKD are unfiltered, while the spectral response of the Y and B channels is determined by a dichroic beamsplitter with a cut-off wavelength of ~500nm. All four channels use high-speed photon counting to generate integer counts in continuous 100μs samples. The resulting time-series are searched for signals at this resolution and at resolutions of selected integer multiples of these samples. Precision photometry is not important, although the data are calibrated to provide reasonably accurate V and B-V values used to confirm the target's identity.

2.1.2. BKD channel

The unique character of the BKD channel deserves close attention. Light reflected by the shiny aluminium of the pinhole diaphragm is reflected again by the pellicle beamsplitter and focused onto the BKD PMT. This provides a roughly 5arcmin diameter annulus that is sensitive to objects moving near the diaphragm. It can be seen in photometry that the BKD field is somewhat off-center relative to the diaphragm, but this does not defeat its purpose. The ratio of the areas (arcmin^2) of the BKD annulus to the diaphragm is 19.26/0.374 = 51.5. If one compares the photometer response in these two fields when pointing at starless regions of the sky, the count rate ratio between the BKD response and the sum of the color channel responses is typically ~2.7. This implies that the BKD sensor is only about 2.7/51.5 = 5.2% as sensitive as the sum of the starlight channels. A similar ratio (=5%) is measured when a star moves from the diaphragm to the BKD annulus.

The fact that the BKD channel geometry captures only a small percentage of incident light does not reduce its importance. Its function is not photometry, but to continuously measure changes in the light surrounding the target star. Its signal includes sky-background, moonlight, stars in the annulus and about 1% of the light of the target star itself. This 1% starlight leakage is attributed mostly to light reflected into BKD by the autoguider, with a small additional contribution due to light scattered by the telescope's primary mirror.

The 1% starlight leakage is important because any variations in the target star brightness will appear, at greatly reduced amplitude, in the BKD channel. For this reason its value is repeatedly measured and verified. The 1% value has been directly measured by comparing the average BKD level when a bright, isolated star is in the diaphragm, to the BKD level measured in a nearby field containing no detectable stars in either the diaphragm or BKD field. Other verifications of this parameter are described later in the text.

2.1.3. Field photography

Not shown in Fig. 2 is a 4-inch refractor (Televue NP101) used for taking 95s exposures of the ~1° field surrounding the target star. These photographs, taken continuously throughout each observation, have often proved vital for identifying the objects seen in the photometry channels. The magnitude threshold in these photographs is typically V~18, sufficient sensitivity for detecting most objects orbiting Earth illuminated by direct sunlight.

2.2. Searching for signals

A single program searches the data from each channel, generating a one-page summary of everything found in the observation. The program treats all channels identically, including BKD, proceeding as follows.

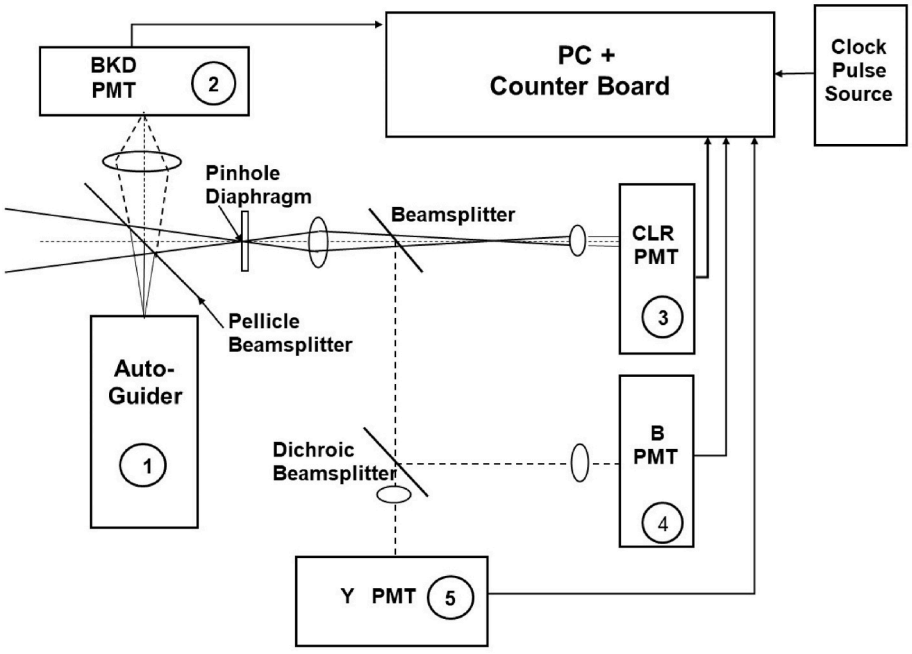

Fig. 1. Schematic of the photometer. Count values from each channel are recorded simultaneously at each clock pulse. The PMTs are Hamamatsu H8259-1,-02, the counter board is National Instrument's NI-6612 and the beamsplitters, optics and mechanical components are stock Edmund Scientific items. Circled numbers identify call-outs in Fig. 2.

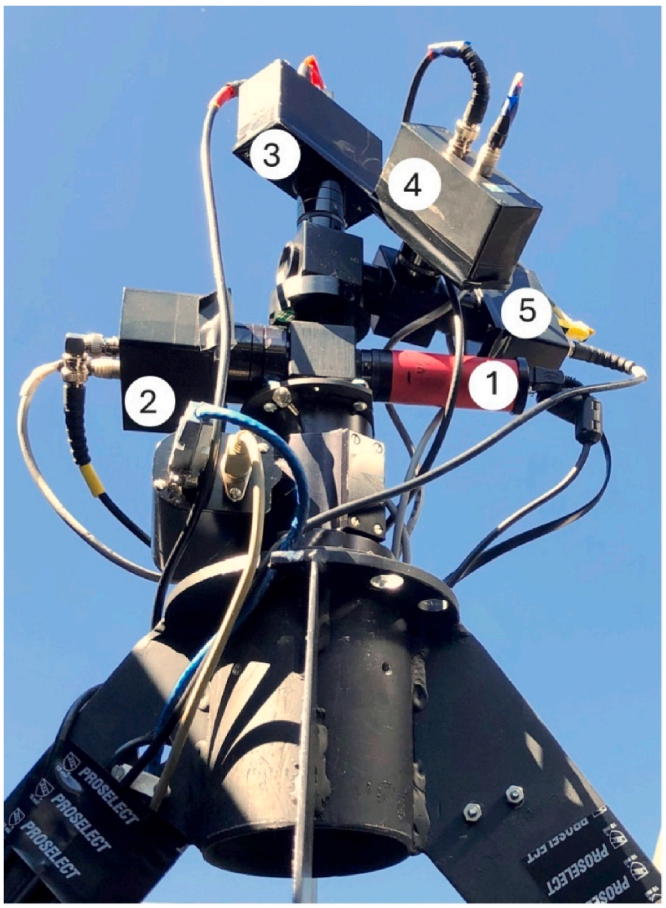

Fig. 2. 4-channel photometer at the prime focus of a 30-inch telescope. For scale, the mounting disk supporting the focuser and photometer is 6 inches in diameter. Call-outs refer to numbers in Fig. 1.

1. Bin the original time-series into six new series, each with samples four times longer than its predecessor. This produces 7 time-series, with resolutions of 100μs to 0.4096s, for each of the four PMT channels (total of 28 time-series).
2. Search each time-series for positive and negative pulses and save the two largest pulses found for each series. Saving only the two largest pulses could miss interesting smaller ones, but experience has shown that smaller pulses are often also detected when they have a longer or shorter duration than the larger pulses. Whenever a bright signal of known origin is found (e.g. an airplane), the search is repeated after the time-series has been truncated to eliminate the bright known source.
3. Search each time-series for frequency peaks in average power spectra generated by repeated FFT transforms. Save the two largest frequency peaks of each time spectrum. As in the case of searching for time-domain pulses, the final pass is conducted with series truncated to eliminate any bright signals of known origin.

The program also generates time-series of 1s and 6.4ms resolution. These have proved valuable for displaying a "quick look" summary of the observation (1s resolution) and for quickly examining any pulses identified by the search process (6.4ms resolution). The original 100μs data are always available to be displayed at any resolution that is an integer multiple of these samples.

2.3. Data display

Many plots of time-series data and frequency spectra are used to illustrate the following sections. Most require manipulations of these data for clear display. Although all such manipulations are listed in the plots, some clarification may be helpful. First, time samples of each channel are read simultaneously but recorded with fixed offsets between the channels of roughly 0.2s. These offsets could be eliminated by a hardware change, but this has proved unnecessary in practice. The offsets are often removed in the following figures for clarity. Other changes include introducing constant vertical offsets between the traces to avoid overlap, and scale changes to bring out features that are otherwise invisible. All modifications for display purposes are listed for each figure in its legend and/or caption.

2.3.1. Quick look data

Fig. 3 shows atypical "quick-look" plot that is displayed for every star observed. These plots give an qualitative overview for identifying problems such as clouds, airplanes or excess noise due to the atmosphere.

2.3.2. Airplanes

Fig. 4 shows a typical airplane passage where both the wing and stabilizer completely block out the target star's light. As is usually the case, the BKD channel picks up one or more of the plane's lights during the passage. The three color channels have been translated in time to show their coincidence, while the BKD channel is offset in time for clarity. Both the CLR and B channels have also been translated vertically to avoid overlap. Note that none of the intense BKD flash is picked up in the color channels, as is usually the case. Data following aircraft passages are often distorted by the planes exhaust/contrail for a few seconds. As this distortion affects both the time and frequency searches, these portions of the time-series are also eliminated prior to the final run of the search program.

2.3.3. Satellites

The passage of an illuminated satellite directly through the photometer's diaphragm is shown in Fig. 5. These events are becoming more frequent with the huge number of satellites being launched for worldwide internet service. The satellite produces a varying signal as it passes through the BKD field and then disappears in that field as it enters the diaphragm. In this case three of the curves have been translated horizontally to display simultaneity and vertically to avoid overlap. The BKD

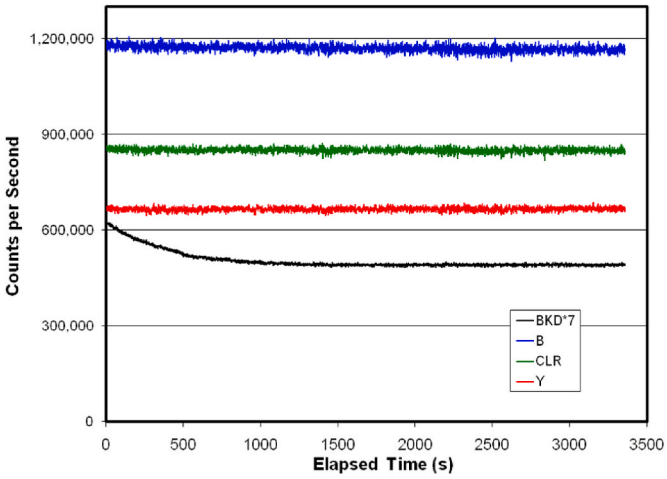

Fig. 3. A 1s resolution time-series of HD89389 on May 14, 2023. The CLR and BKD channels are unfiltered, B covers the blue end of the spectrum, cut off at 500 nm by the dichroic beamsplitter, and Y the red end. No vertical or horizontal offsets have been made in this plot. BKD counts have been multiplied by 7 to increase visibility of the fading twilight. (For interpretation of the references to color in this figure legend, the reader is referred to the Web version of this article.)

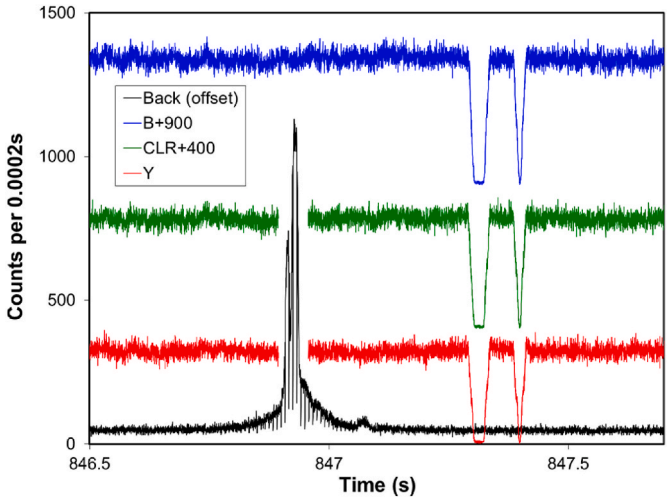

Fig. 4. Airplane passage illustrating use of both time and vertical offsets for clarity. The BKD signal shows the effect of high frequency modulation present in some airplane lights.

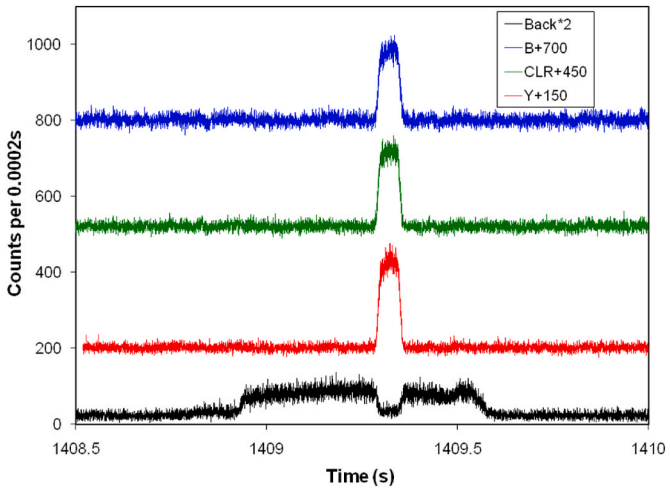

Fig. 5. Satellite passage through BKD field and diaphragm (HD187637 on Sep 19, 2023). These data enable measurement of both the sensitivity of the BKD channel and the amount of light leaked from the target star into the BKD PMT.

trace is increased by a factor of two for clarity. None of these events have ever displayed a dip in the target star's light, an indication of the small size of the satellite's shadow.

The information recorded in this event serves as a Rosetta Stone for decoding details of the BKD channel sensitivity. The following numbers are average counts per 0.0002s (raw data binned by 2x) measured during this event.

1. BKD before satellite appears: 11.576 per 0.0002s
2. BKD when satellite is in the 5′ annulus approaches diaphragm = 46.603, an increase of 30.027
3. Total count rates (sum of three colors): Star = 224.681, Satellite = 825.967–224.681 = 601.286
4. BKD increase when both star and satellite are in diaphragm: 6.0615 (=17.6375–11.576).

These numbers provide accurate measurements of two key parameters discussed previously (Sect, 2.1.2).

5. Fraction of the satellite's light measured when it crosses the BKD field = 30.027/601.286 = 0.0499 (5%)
6. Fraction of the satellite's light added to BKD when centered in diaphragm = 6.0615/601.286 = 0.01008 (1%).

2.3.4. *Meteors*

Fig. 6 shows the passage of a Perseid meteor through the BKD field and diaphragm. If a point object moves from the diaphragm to BKD, the BKD signal is much smaller (5%) than the sum of the three color channels. In Fig. 6 the peak BKD is much larger than expected, reaching 4 million photons per second. Apparently, only a portion of the meteor's light was captured in the diaphragm, while the larger BKD field saw more of the passing fireball.

2.3.5. *Birds*

The signal believed caused by a large bird, perhaps by one of our bald eagles, is plotted in Fig. 7. The dip corresponds to ~30% of the mirror area being eclipsed. Note that the light level never increases due to reflected light or any other source. Events attributed to birds are much less common than those of airplanes or satellites.

2.3.6. *Frequency spectra*

A final example, Fig. 8, illustrates the power of the spectral analysis in finding weak periodic signals. In this case, a 2500s observation of the Crab Pulsar and surrounding nebulosity was analyzed with 3.2ms time resolution. Ninety-nine percent of the light detected was from sources other than the pulsar: 50% from the nebula, 45% from moonlight and skylight and 4% from a nearby star. When 731 individual FFT spectra were combined, the background noise was dramatically reduced, yielding the spectrum in Fig. 8. Note that the 30Hz fundamental is accompanied by a number of large harmonics, consistent with the known non-sinusoidal shape of the Crab Pulsar light curve.

2.4. *Noise sources*

There are two mechanisms that account for essentially all of the noise in this photometry: Atmospheric scintillation and statistical counting noise. Dark current and its associated noise are neglegible. Counting noise ("shot noise"), inherant in counting random events, determines the minimun noise floor in all observations.The contribution of the atmosphere can be much larger than this floor, particularly at low frequencies.

An example of noise due to atmospheric scintillation on a night of poor seeing is displayed in Fig. 9. The intensity of scintillation noise can vary from night to night and even hour to hour. It can be reduced by

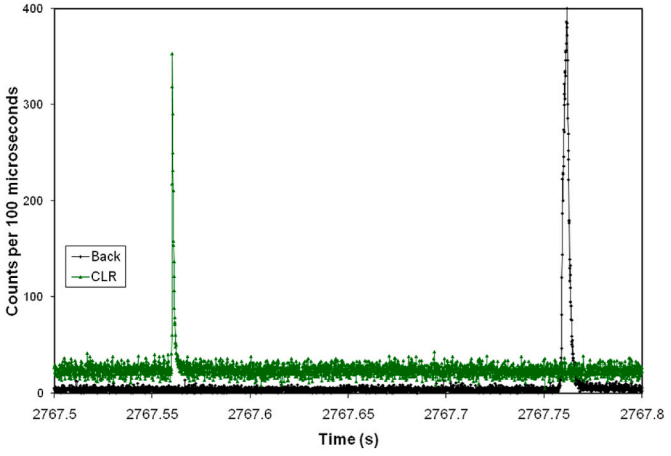

Fig. 6. CLR and BKD channels of a Perseid meteor. The offset in time is due to the fixed delay recording samples. The intense BKD signal is due to a fireball that is evidently much larger than the diaphragm.

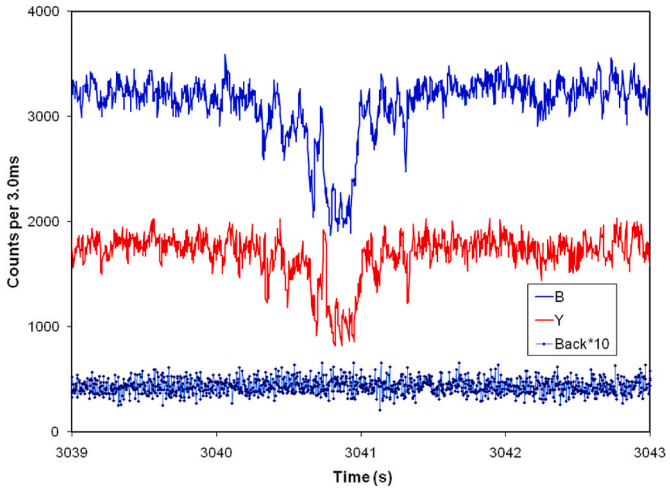

Fig. 7. Photometry of a probable bird passage, showing a significant dimming of the target star but no increases due to reflected light from the surroundings.

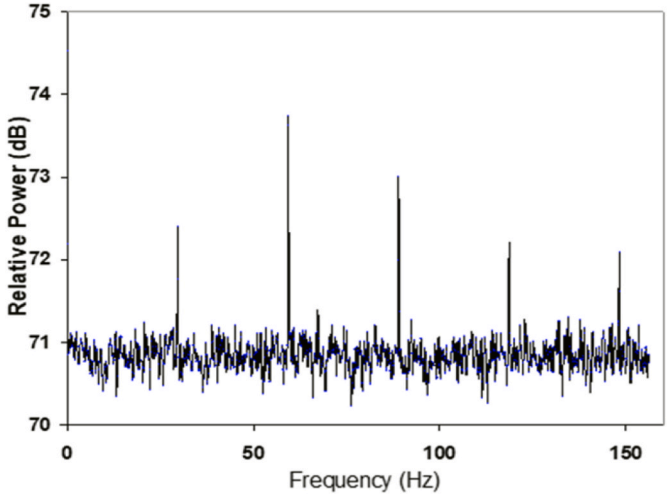

Fig. 8. Frequency spectrum of the Crab Pulsar on March 31, 2017. The faint pulsar contributes only 1% of the light entering the diaphragm, but is easily detected by its constant 30Hz optical tone.

observing stars higher in the sky or using a larger telescope [8]. The difference between a night of good "astonomical seeing" and an average night can be quantified by examining the power spectrum of the star's light during an observation.

2.4.1. *Scintillation power vs. frequency*

Frequency spectra are calculated for all channels during data processing. Fig. 10 shows the power spectrum of both the star (CLR channel), and the BKD channel during the observation of HD89389. The horizontal segments of these curves correspond to frequencies where the contribution of the atmosphere is negligible, leaving only statistical counting noise in the spectrum. Atmospheric scintillation is always present at low frequencies, limiting the size of slow signals that can be reliably detected. On this night the atmosphere was quite calm, adding essentially no power to the spectrum above 70Hz.

There was significantly more atmospheric scintillation power during the observation of HD217014. As can be seen in Fig. 11, the atmosphere is adding noise even at 200Hz on this night.

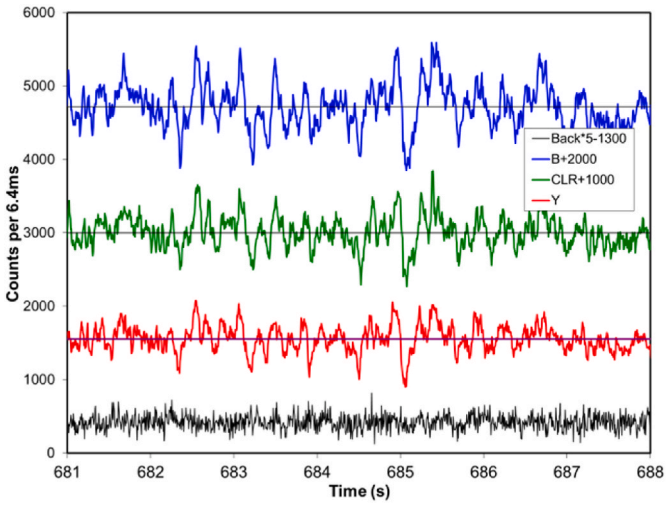

Fig. 9. Noise due to atmospheric scintillation (seeing) is present in every observation. Good nights can usually be identified by the lack of bright star twinkling to the eye.

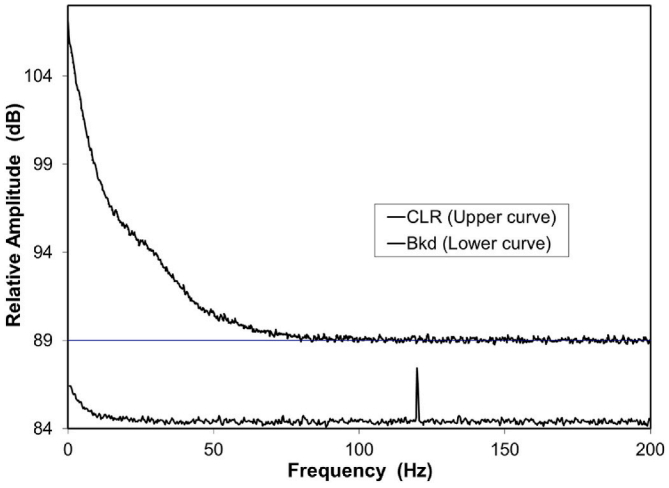

Fig. 10. Scintillation power spectra during good seeing (May 14, 2023). The level section of these curves is due to statistical noise (shot noise) when the contribution of the atmosphere is negligible. The spike at 120Hz in BKD is visible on most nights, caused by the nearby light pollution.

2.5. *Field photography*

Fig. 12 illustrates a typical exposure taken of the star-field surrounding a target during an observation. Thirty-five identical exposures were taken during the 56-min observation of HD89389. The target star is in the center of this roughly 15 × 20arcmin field. The strange pulses described in the next section occurred during this 95s exposure. The faintest stars detected consistently in every photograph are about magnitude V = 18. A careful examination was made of each photograph to detect any streaks or transitory point images that might have been objects moving through the field. Nothing was found in any of these frames, suggesting that the source of the pulses was either invisible, such as due to some atmospheric effect, or too far away to be detected.

Satellites are frequently seen in these photographs. Fig. 13 illustrates an example one of the more distant objects that are easily detected. Although 35,786km above Earth, geosynchronous satellites are often seen when the target stars are near −5.5° declination. Objects this far away are almost always illuminated in full sunlight, a factor important in deciding what may, or may not, have pass though the field. Note that

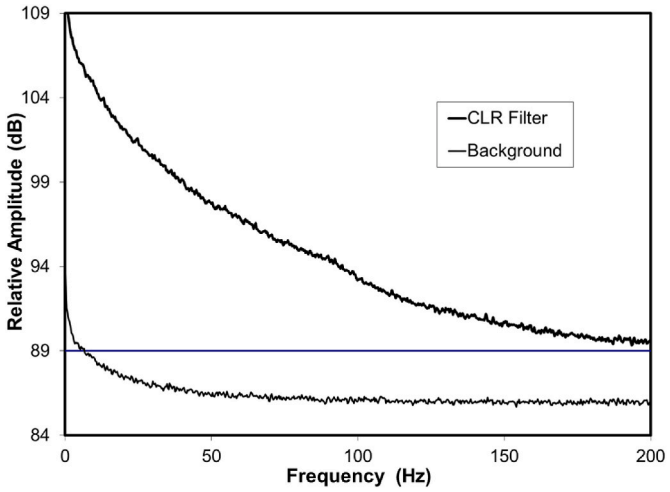

Fig. 11. Atmospheric scintillation during the observation of HD217014. The increased scintillation power on this night did not seriously degrade the detected pulses since their short duration moved much of their frequency content to the higher, less affected, frequencies.

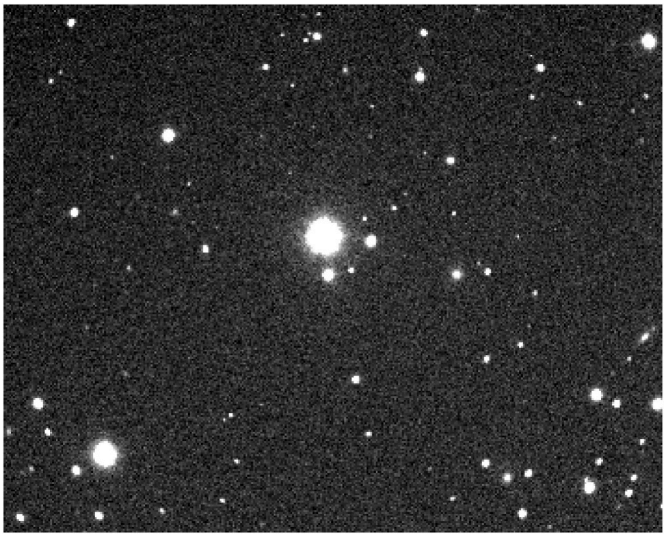

Fig. 12. A ~15 × 20arcmin unfiltered photo of stars surrounding HD89389 taken simultaneously with the appearance of "strange" pulses described below. Nothing was seen moving through this field in any of the 35 frames taken during this observation.

objects in the atmosphere or in low Earth orbit are often not illuminated by sunlight.

3. Strange pulses

3.1. Initial discovery

A very unusual pair of optical pulses was found as the search program delved through the data shown in Fig. 3. An examination of the 6.4ms time-series at the time identified by the program revealed two identical pulses where the star brightness rapidly increased–decreased–increased in a fraction of one second (Fig. 14). The first pulse occurred1455s after the start of the observation on May 14, 2023; the second pulse arrived 4.42s later. The small ripples in the BKD channel are entirely consistent with the starlight leakage into this channel discussed in Sections 2.1.2 and 2.3.3.

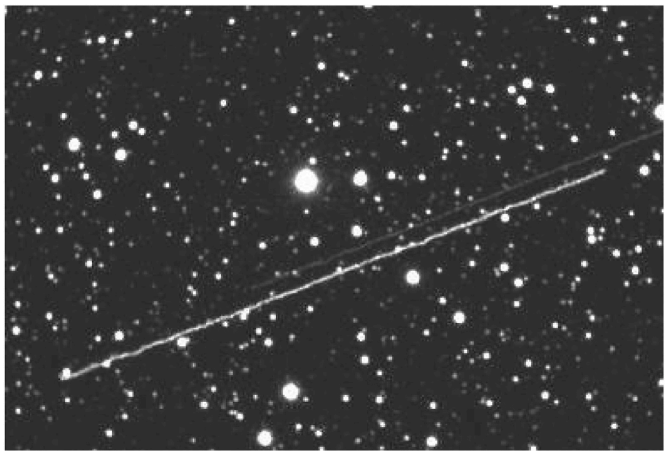

Fig. 13. Distant geosynchronous satellite passing the star HD52265 illustrates the 4-inch telescope's sensitivity to orbiting objects (exposure = 95s, FOV 18′×26′). Although these satellites are large, the strength of this trace suggests that smaller objects could be detected at this distance (35,786km). A satellite orbiting even farther away would be moving more slowly, possibly still detectable as its light would be spread over fewer pixels.

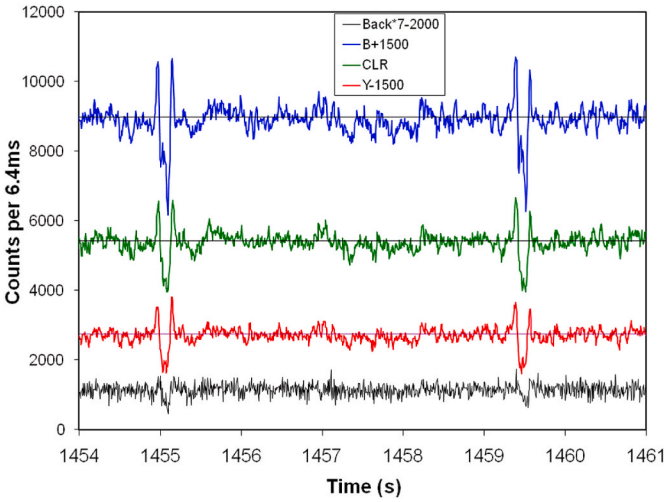

Fig. 14. Strange pulses in the light of HD89389 on May 14, 2023. The first pulse appeared at 9:12:44 PDT, and the second pulse arrived 4.42s later. The raw data have been shifted to line up in time and vertically to avoid overlap. The raw BKD intensity has been multiplied by 7 and then shifted vertically to improve visibility.

3.1.1. Pulse characteristics

Several unusual characteristics of these pulses should be noted.

1. No single pulse anything like these has ever been found in more than 1500 hours of searching.
2. The star's light is attenuated by ~25% in a tenth of a second. This is much too fast to attribute to any known phenomenon at the star's distance. Light from a star a million kilometers across cannot be attenuated so quickly.
3. During the 4s interval between the pulses, the starlight is essentially unchanged in intensity, color and RMS noise from conditions before and after this event.
4. The increase and decrease in starlight during each pulse eliminates "common signals" such as generated by airplanes, satellites, meteors, and strobe lights from the list of possible causes.
5. The star never completely disappears, unlike during a typical airplane or asteroid occultation.

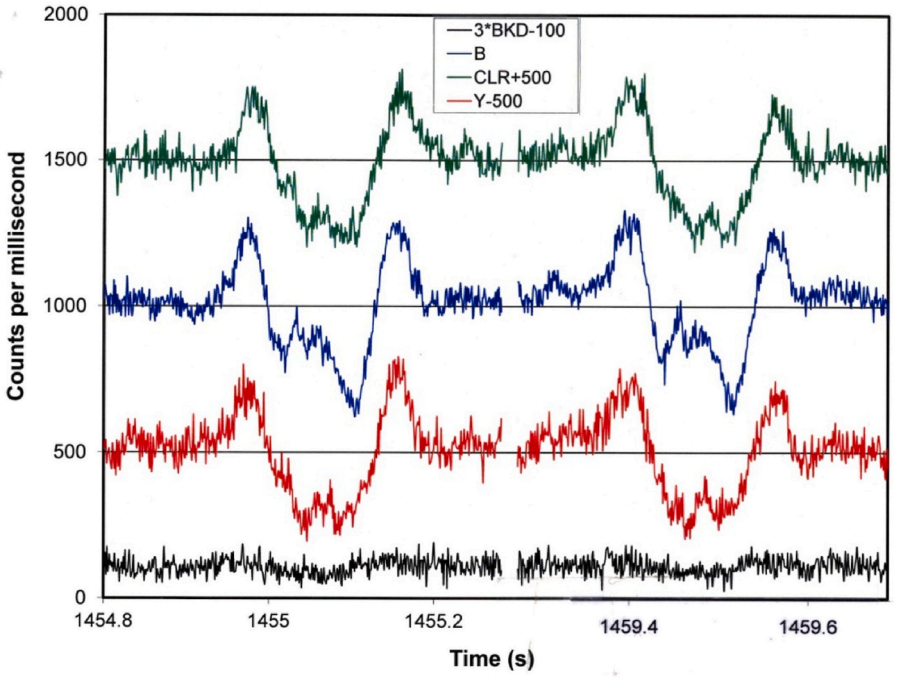

Fig. 15. Close-up of the HD89389 pulses with time resolution increased to 1ms. The three color curves have each been normalized to an average value of 1000 and then offset vertically for visibility. The two pulses have been brought together for comparison by deleting most of the data between them. Note that the light variation at minimum repeats for each color with remarkable accuracy. (For interpretation of the references to color in this figure legend, the reader is referred to the Web version of this article.)

3.1.2. A closer look

Fig. 15 gives a closer look at the pulses in Fig. 14. The time resolution in this view has been increased to 1.0ms and the second pulse moved close to the lead pulse for comparison. The three-color channels have been normalized to the same average intensity (1000/ms), making differences between the variations in different colors more evident. Two additional details are clear in these plots.

1. Significant differences between the color channels are seen in the structure of the light between the peaks. This is particularly noticeable in the B channel.
2. This "fine-structure light" is reproduced with remarkable accuracy in the second pulse of the same color. In order to be preserved over an interval of more than 4s, this variation must be real, not noise.

3.1.3. Analysis

3.1.3.1. How is the starlight between the pulses affected by this event?. The average value and standard deviation are calculated for a 5s interval before the first pulse, a 3s interval between the pulses and for a 5s interval after the second pulse. The results are compared in Table 1. The average values for each color differ less than 2% from each other, indicating that no significant change occurs in the starlight intensity between the pulses. The standard deviation calculated for all three color channels is 4–7% larger between the pulses than the average. This is likely due to variation in atmospheric scintillation in the relatively short data segments available between the pulses.

The next two lines in the table measure the depth of the largest valleys of each color channel and compare them to the average standard deviation for that channel. It should be no surprise that the signal-to-noise of the detected pulses greatly exceeds what can be expected from random noise.

3.1.3.2. Are the pulses seen in the BKD channel consistent with starlight leakage?. The depth of the valley of both pulses is calculated for each color, and the sum of these depths compared to the depth measured in the corresponding BKD trace. An average of the ten lowest points is used to reduce noise. The results of this calculation (Table 2) show that the depths of the BKD pulses are 1.38% and 1.15% of the sum of the starlight channel depths for the first and second pulses, respectively. These values are consistent with the known 1.0% starlight leakage from the target star into BKD.

If the depth of the BKD pulse had the same relative amplitude as the star channels, one might argue that something is simply flying over the telescope and blocking roughly 25% of the telescope's aperture. A comparison of the minima in each of the four channels shows that this is not the case. The numbers for BKD (13% and 10% in Table 2) are about a factor of two smaller than for the star channels (21%–26%). Since the other sources of the BKD light (skylight and faint stars in the BKD field) are not affected by the changes in the star's light, this amplitude difference strongly implies that the source of these pulses cannot be caused simply be something blocking out part of the telescope aperture.

3.2. A second event is found

A very similar event was found during a re-examination of earlier observations. Pulses in the light of HD217014, a star in a completely different part of the sky, had been found nearly four years earlier on Sep. 30, 2019, but ignored as likely being due to a formation of birds. This "second" event occurred 2057.8s after the start of the observation at 8:24:03 PDT. The second pulse arrived 1.283s later. Data from this observation are plotted in Fig. 16. Note that while the pulse separation is 3.5 times less than for the HD89389 event, the bipolar pulse shapes and separation look very similar. In fact, separation between pulses is roughly 20 times the pulse duration for both events.

Almost all characteristics noted above for HD89389 are present in the HD217014 light curves. However, the high-resolution view with the two pulses brought close together (Fig. 17) shows a complete absence of the "fine-structure light" that is so prominent in Fig. 15.

Table 1
Statistical analysis of pulses (raw data, not re-scaled).

	Y	B	CLR	BKD
Average Value				
5s before	4268	7527	5463	448.9
3s between pulses	4221	7417	5417	448.8
5s after	4265	7535	5485	450.1
Average:	4251.3	7493.2	5455.0	449.3
Standard Deviation				
5s before	144	238	176	22.1
3s between pulses	151	271	197	22.1
5s after	142	250	188	22.7
Standard Deviation Ave	145.8	252.9	187.2	22.30
Deepest Valley	−1125	−2792	−1471	–
S/N of Deepest valley	7.7	11.0	7.9	

Table 2
Comparison of the valley depths (raw data, not rescaled).

Pulse 1 Valleys	Y	B	CLR	BKD
Valley10-point average	3298.5	5529.8	4129.7	390.5
Average Level	4251.3	7493.2	5455.0	449.3
Average Valley depth	−952.8	−1963.4	−1325.3	−58.79
% of Average level	−22.4	−26.2	−24.3	−13.1
BKD/(Color Sum)	0.0138			
58.8/4242 =				
Pulse 2 Valleys				
Valley10-point average	3358.0	5742.8	4145.9	404.0
Average Level	4251.3	7493.2	5455.0	449.3
Average Valley depth	−893.3	−1750.4	−1309.1	−45.3
% of Average	−21.0	−23.4	−24.0	−10.0
BKD/(Color Sum)	0.0115			

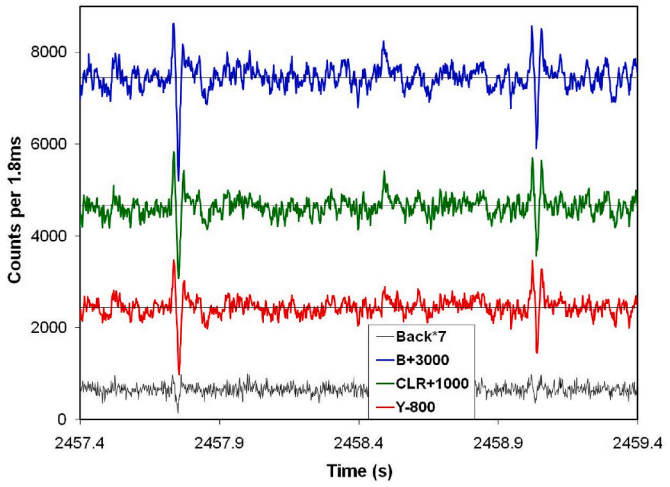

Fig. 16. Pulses in the light of HD217014 on Sep. 30, 2019. Time resolution is 1.8 ms, 3.5 times faster than in Fig. 14.

3.2.1. *HD217014 analysis*

Data displayed in Fig. 16 were analyzed in Tables 3 and 4 using the same approach as in Tables 1 and 2 The first pulse of this event shows the largest changes relative to the ambient starlight level, 40%–45% decreases; the second pulse was significantly smaller (26%–32%). Although the relative percentage drops in the BKD channel (32.1% and 22.5%) are larger than for HD89389, the calculated percent of the star's light in BKD (1.09% and 1.10%) is again consistent with the BKD pulses being due completely to starlight leakage, mostly due to light reflected by the autoguider.

4. What might have caused these pulses?

Six possible mechanisms have been suggested.

1. Birds or some other object flying near the telescope
2. Shock waves in our atmosphere
3. Diffraction by distant edges
4. Partial eclipses by orbiting bodies
5. Passing gravity waves
6. Influence of extraterrestrial intelligence

4.1. *Birds or other nearby object*

The HD217014 event was initially dismissed as "birds" because no other explanation seemed to fit. The thought was that perhaps a flock of birds flew through the field, illuminated by some light source on the ground (there was no moonlight). This theory is considered wrong for several reasons.

1. Illumination sufficiently intense to produce the observed light peaks would have been easily detected by the BKD sensor. This light would have produced a completely different time signature than what is observed, as is the case when satellites or airplanes pass through the field.
2. Nothing was detected moving through the photograph taken during the HD89389 event (Fig. 12).
3. None of the bird signatures identified to date have *increased* the star's intensity, and all occur as single events, never in pairs (e.g. Fig. 7).

The same objections apply to the model of an opaque object partially occulting the telescope aperture. A linear object, such as a wing could be no wider than six inches to account for the observed fading of the star. The difference in the attenuation of the star's light between the color channels and BKD eliminate this possibility (Sect. 3.1.3.2).

4.2. *Atmospheric shock wave*

Could the observed pulses be generated by refraction by our atmosphere? The atmosphere is capable of intensely modulating starlight in all colors. Although such strong scintillation seems to invariably produce random modulation, as seen in Fig. 9, this experience does not prove that the observed pulses could not be generated by an atmospheric disturbance, such as a shock wave. Since the speed of sound in air is relatively constant, one would have to explain two events of such different time scales.

4.3. *Starlight diffraction by a distant edge*

Diffraction of starlight by a distant body can produce modulation similar to that observed. This possibility is examined in more detail in Section 5.

4.4. *Partial eclipses by orbiting bodies*

Could satellites orbiting Earth or distant asteroids generate these signals? An increasing number of asteroids have been found to have orbiting companions using radar and occultation measurements [9]. Perhaps a fortuitous alignment of these bodies could explain a double pulse event. But it seems highly unlikely that two cases of nearly identical pulses would be found. A similar argument applies to Earth-orbiting satellites, which are much less likely to cast a detectable shadow on the telescope.

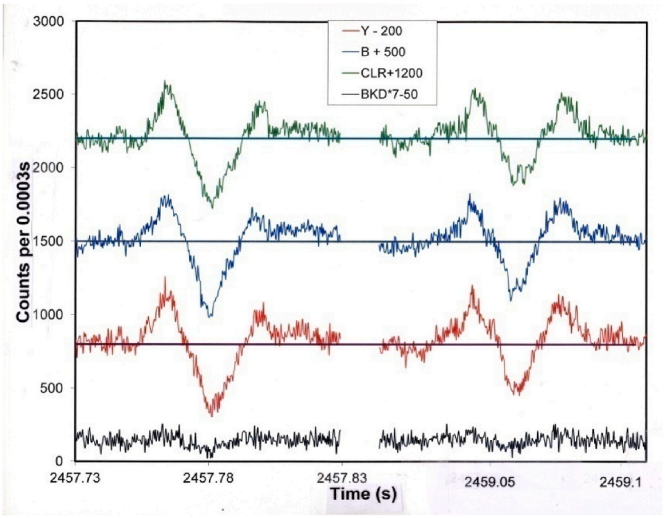

Fig. 17. Close-up of the HD217014 pulses with time resolution increased 0.3ms. Pulses have been brought together by deleting most of the data between them. The three color curves have each been normalized to an average value of 1000 and then separated vertically by 700. Note the absence of "fine structure light" at minimum. (For interpretation of the references to color in this figure legend, the reader is referred to the Web version of this article.)

Table 3
Statistics of the HD217014 event (raw data, not scaled).

	Y	B	CLR	BKD
	Average Value			
1.6s before	1811.8	2486.9	2049.0	91.82
0.9s between pulse	1813.5	2474.2	2020.3	91.92
1.6s after	1788.3	2471.1	2032.3	91.89
Average:	1804.5	2477.4	2033.9	91.88
Standard Deviation				
1.6s before	84.0	114.9	92.4	10.1
0.9s between pulses	88.4	123.0	108.7	10.2
1.6s after	87.8	105.9	100.8	10.0
Standard Deviation Ave	86.7	114.6	100.6	10.1
Deepest Valley	−842.5	−1264	−920.9	–
S/N of Deepest valley	9.7	11.0	9.2	

Table 4
Comparison of HD217014 valley depths (raw data).

Pulse 1	Y	B	CLR	BKD
Valley5-point average	1053.2	1351.0	1202.0	62.4
Average Level	1804.5	2477.4	2033.9	91.88
Average Valley depth	−751.3	−1106.4	−831.9	−29.5
% of Average	−41.6	−45.5	−40.9	−32.1
BKD/(Color Sum)	0.0109			
Pulse 2				
Valley5-point average	1264.8	1661.2	1505.2	71.20
Average Level	1804.5	2477.4	2033.9	91.88
Average Valley depth	−539.7	−816.2	−531.7	−20.7
% of Average	−29.9	−32.1	−26.1	−22.5
BKD/(Color Sum)	0.0110			

4.5. Passing gravity waves

The intriguing possibility that a gravity wave might have generated these pulses deserves closer examination. Analysis of this idea is beyond the scope of this paper and left to future investigators.

4.6. Influence of extraterrestrial intelligence

Whatever is modulating the star's light must be relatively close to Earth, implying that any ETI activity must be within our solar system. Perhaps an ETI connection can be made once additional observations using arrays of optical telescopes provide data that more fully explains what is causing these pulses (Section 5.7).

5. Edge diffraction

It has been known since the 17th Century that collimated light diffracted by a straight edge produces ripples in the shadow of that edge. Many of the best scientific minds in the 18th and 19th centuries struggled to explain this effect, culminating in Sommerfeld's mathematical derivation based on the wave nature of light [10].

5.1. Astronomical examples

Two photometric observations made by the author illustrate this phenomenon. The first shows the occultation of 75 Tau as the Moon moved through the Hyades star cluster on March 4, 1979 (Fig. 18). Without diffraction the star would have quickly disappeared in about 5ms as the limb passed over it. Instead, light diffracted by the Moon's limb produced intensity ripples long before the limb reached the star. Note also that the star's light slowly decreases after the peak is reached, a rate determined by diffraction, not by the size of the star.

Occultations by known asteroids are also observed in events predicted by the International Occultation Timing Association (IOTA) [11]. Such a case is shown in Fig. 19, an occultation on Nov. 11, 2014 of the star TYC 1397-297-1 by the 50km asteroid, Eugenisis. Note that both the leading and the trailing edges of the occultation exhibit diffraction peaks.

5.2. Factors affecting the diffraction curve

The shape of the peaks in Figs. 18 and 19 generally match the theoretical curve for diffraction, Fig. 20, calculated using Fresnel's integrals for a single wavelength of light [12]. The horizontal scale has been adjusted to the size of the diffraction pattern in Fig. 18, projected on Earth's surface. The theoretical fringe pattern continues indefinitely with successive peaks and valleys of gradually decreasing in amplitude. Only the first peak is shown in Fig. 20 since five important factors can limit and distort this pattern in astronomical photometry. Many of these factors are discussed by Warner [8] in his chapter on the use of lunar occultations to measure the diameter of giant stars.

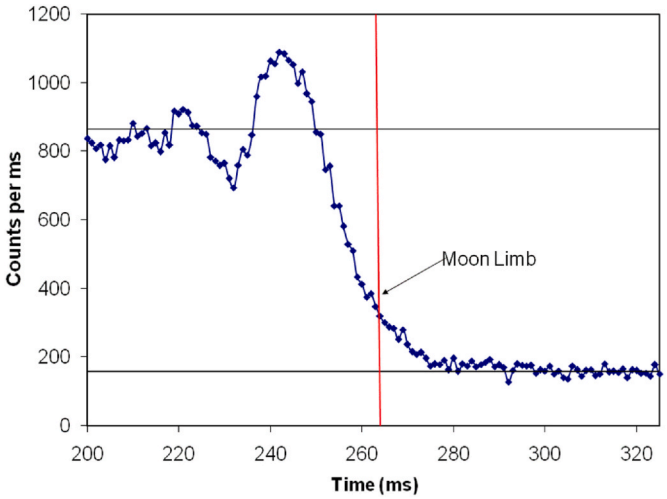

Fig. 18. Diffraction during occultation of 75Tau by the Moon. Taking into account the angle of the Moon's limb relative to its velocity (37°), the measured peak width (14ms) corresponds to ~8.4m on the Earth's surface.

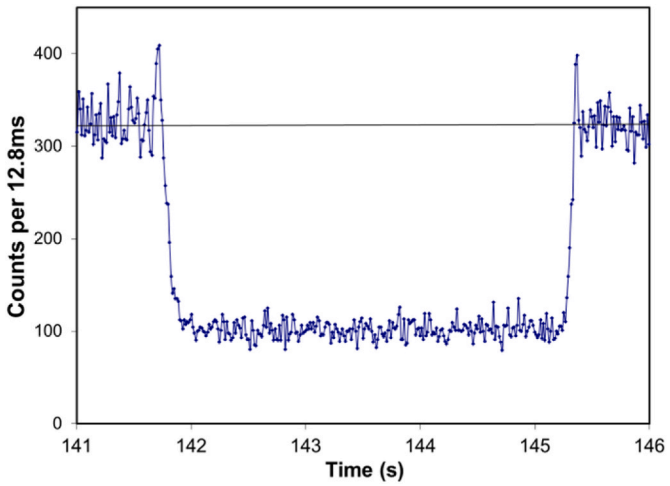

Fig. 19. Observation of edge diffraction during an occultation by the 50km asteroid Eugenisis. The distance to the asteroid at the time was 268 million kilometers.

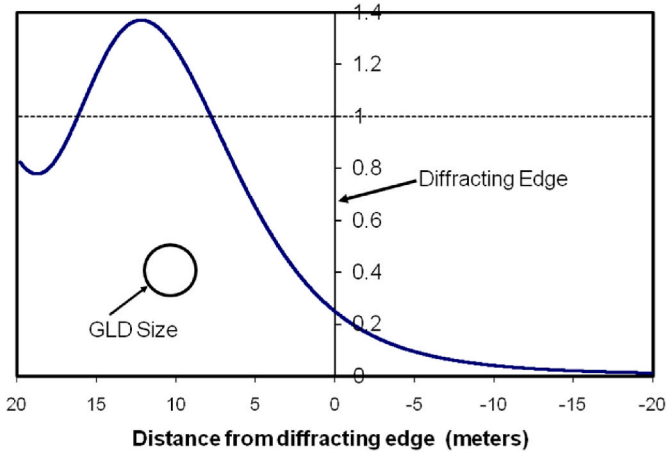

Fig. 20. Theoretical diffraction curve for a single optical wavelength. Vertical scale is intensity relative to the undiffracted light. The horizontal scale shows the size of this pattern on Earth's surface generated from the Moon's distance. The GLD for the star occulted in Fig. 18 is drawn to the same scale in meters, showing that it is less than half the width of the diffraction peak.

1. Broadband photometry causes the patterns of different wavelength to overlap. Since the size of the fringes varies with wavelength, this overlap quickly smears out the higher order peaks.
2. Atmospheric scintillation always adds noise, distorting the observed pattern.
3. Deviation of the diffracting body's limb from a straight edge could distort the diffraction pattern. This problem is rarely observed in diffraction by the Moon since the lunar limb is generally quite smooth over distances of tens of meters.
4. The finite angular diameter of the star also distorts the fringe pattern. As the apparent diameter of the star increases, the pattern amplitude decreases and eventually is lost.
5. If the width of the first diffraction peak, is smaller than the telescope aperture, averaging by that aperture smoothes and distorts the measured photometric pattern.

The first three factors are ignored in the following paragraphs, assuming 1) that the wide spectral band pass used effectively limits the diffraction pattern to the first fringe, 2) that the atmosphere is sufficiently stable for performing a reasonable fit and 3) that the diffracting edge is sufficiently straight to provide good diffraction. Under these conditions, factor #5 sets a lower limit on range of about 3300km (500nm light). Although fringes might be detected at half this range, airplanes and satellites in low Earth orbit are simply too close to generate a detectable pattern.

Factor #4 defines an upper limit on target range. Nather and Evans [13] developed theoretical light curves for diffraction by the Moon showing the degradation expected as a function of the apparent size of the diffracted star. If the star's diameter is less than 0.005arcsec, the effect relative to a point source is mainly a reduction in amplitude of the diffraction peaks. Diameters larger than this increasingly cause attenuation and distortion of diffraction pattern. A 0.005arcsec disk at the Moon's distance would be 9.3m across. This is close to the width of the first diffraction peak projected on the Earth's surface (8.4m). This result suggests that the diffraction pattern becomes weak and distorted when the apparent diameter of the star, translated to a linear dimension at the Moon's distance, becomes larger than the width of the first diffraction peak, measured on the ground. In the remainder of the paper this rule is assumed to apply to diffraction generated by objects more distant than the Moon.

5.3. Geometric Light Disk

In order to illustrate the constraint on the maximum distance due to apparent star diameter, the following sections make use of a construct called the Geometric Light Disk (GLD), defined as the size of an opaque disk that would completely block a star's light from the observer, ***in the absence of diffraction***. For large distances, the size of this disk is clearly a linear function of its distance. If relatively close, the telescope's aperture determines its size. If the disk is as far away as the star, its diameter would be as large as the star itself. In practice, the size of this disk can be compared to the size of a diffraction pattern falling on the ground from the distant object. If the GLD is larger, Factor #4 dominates, and the object is too far away to generate a clear diffraction pattern. The circle marked "GLD" in Fig. 20 shows the projected size of the star that generated the fringes in Fig. 18, on the same scale as the diffraction pattern, illustrating that in this case the GLD is small enough to generate the clear diffraction pattern that was observed.

5.4. Fit of edge diffraction to observed pulses

Fig. 19 suggests a model for deriving the shape of the observed pulses. If the length of the Eugenisis occultation is shortened to eliminate the totality phase, perhaps the resulting light curve would resemble the observed pulses. Since diffraction depends on having a long edge, this shrinkage must occur in a way that retains a sufficient length of edge. This suggests that the observed peaks could be generated by diffraction of two edges on either side of an opaque bar. As the star approaches the first edge, light is diffracted towards the observer from along the bar's edge, producing a well-defined light peak. As it moves even closer, some of the starlight is diffracted away, giving rise to a gradual dimming. Then, as the star emerges on the other side of the bar, this light variation is repeated in reverse.

To test this model, Fig. 21 matches this theoretical curve for a single wavelength with the observed shape of the HD89389 (first pulse) and HD217014 (second pulse) in all three color bands. The horizontal scale and position of the theoretical curves are fitted, respectively, to the observed width of the first diffraction peak and the time that the descending light crosses the 100% starlight level. The vertical scale is adjusted to match the 100% level to the star's ambient light.

Although the fits to the observed pulses in the Figure are far from perfect, it is interesting that the roll-off in intensity from the peak to minimum fits quite well, particularly for the HD217014 pulse. Imperfections in this fit, including the lack of higher order peaks, could be due to the five distorting influences listed above, particularly to the use of a broad spectral band for these measurements. Table 5 summarizes the fit

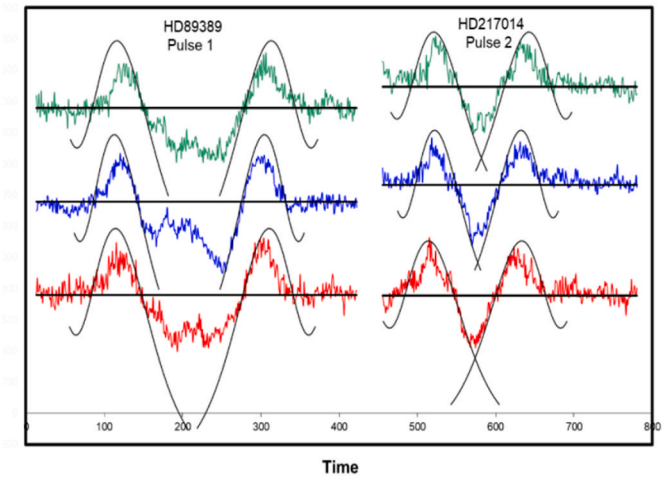

Fig. 21. Fit of the diffraction curve for a single optical wavelength (Fig. 20) to the first pulse of HD89389 and the second of HD217014. Units are omitted to enable different time scales to be displayed on a single graph. The parameters used for the curve fits (seconds) are given in Table 5.

Table 5
Diffraction fit results (seconds)—spacing is between 100 % level crossing.

Peak:	Width	Spacing	Width	Spacing
HD89389:	Pulse 1	Pulse 1	Pulse 2	Pulse 2
Y	0.0645	0.129	0.062	0.122
B	0.056	0.133	0.053	0.130
CLR	0.065	0.129	0.059	0.129
HD217014				
Y	0.0168	0.022	0.0190	0.016
B	0.0153	0.020	0.0156	0.018
CLR	0.0156	0.020	0.0180	0.018

Table 6
Star Characteristics-Star physical diameter is estimated based on spectral class.

Star	Spectrum	V Mag	Distance (LY)	Diameter (10^{-9} Rad)
HD89389	F8V	6.45	105	1.6
HD217014	G5V	5.45	51	3.3
75 Tau	K1III	4.97	193	8.4
TYC 1307-00297-1	G5?	11.45	460	0.29

parameters used for the pulses of both events. Table 6 lists the estimated apparent diameter and other relevant parameters of the stars discussed here.

5.5. Growth of diffraction pattern with distance

The size of a diffraction pattern projected on Earth by a point source illuminating a distant edge can be calculated as a function of wavelength, λ, and the distance, D, between the diffracting body and the screen (e.g. Earth surface). Assuming a flat screen and normal incidence, the projected distance, d, to the peaks and valleys of a diffraction pattern is given by

$$d = \sqrt{\lambda D(m + 3/4)} \quad (1)$$

where m is the number of the maxima (even m) or minima (odd m) [14]. Only the first maximum, m = 0, is considered. The width of this peak can be used as a single parameter measurement of size of the diffraction pattern since it can be measured in time-series photometry. This width is 69% of d(m = 0) or

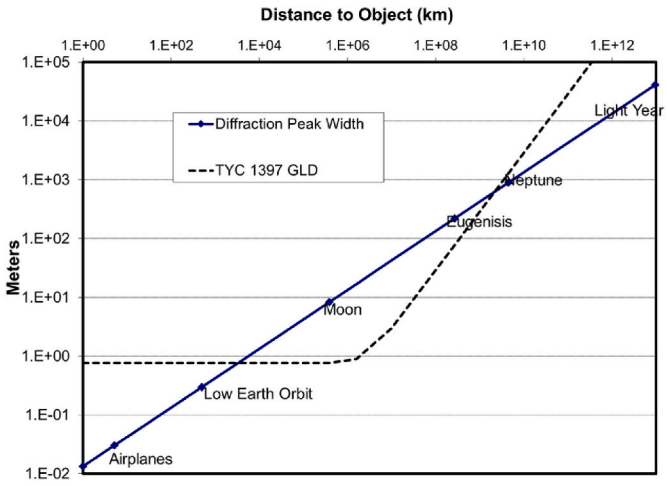

Fig. 22. Diffraction peak width and GLD size vs. distance. It is assumed that the diffraction pattern is too degraded when the GLD and the size of the first diffraction peak, measured on Earth, are equal.

$$w = 0.69\sqrt{3\lambda D/4}\,. \quad (2)$$

Peak width in meters is plotted as a function of distance D in kilometers, for a wavelength of 500nm, in the solid curve in Fig. 22. Note that the diffraction pattern grows slowly as the square root of distance, while the GLD (dashed line) grows linearly once it is larger than the telescopes aperture. The GLD is plotted for TYC 1397-297-1, the star occulted by Eugenisis. Note that the assumption that the star GLD is small relative to the size of the diffraction peak doesn't break down until reaching Neptune, due to the small size of this star. For closer stars such as HD89389 and HD217014, the maximum range shrinks considerably, due to their larger apparent diameter.

5.6. Estimating distance to diffraction source

In order to measure the actual distance, rather than just a range of possible values, one needs to measure the size of the diffraction peak as it moves across the ground. This measurement becomes tractable if, instead of measuring the pattern dimensions, one measures the speed that the pattern moves. The predicted curve of diffraction peak size vs. distance can be transformed into speed vs. distance by dividing by the pulse length (time) measured in the photometry.

Equation (2) can be written in terms of shadow velocity, v, and measured pulse length, t,

$$v = w/t = (0.69/t)\sqrt{3\lambda D/4} \text{ or}$$

$$D = 2.80(vt)^2/\lambda \quad (3)$$

The speed that the lunar shadow moved across the ground in Fig. 18 is estimated using the Moon orbit speed (1.0 km/s) and subtracting the eastward motion of the observatory due to Earth's rotation (~250m/s). We know from the geometry of this event that the limb was moving over the star at an angle of ~37° with respect to its normal. Using this measured ground speed, v = 750cos(37°)m/s, the measured peak duration, t = 14ms, and λ = 500nm, the calculated distance to the moon is 395,000km, very close to the ephemeris distance at the time of 391,595km.

For the Eugenisis case, the shorter of the two peaks in Fig. 19 (38ms) is selected, assuming that this corresponds to near normal encounter between the star and asteroid limb. The shadow ground speed (6737m/s) and asteroid distance (286×10^6km) are known based on predictions provided by IOTA. Assuming motion normal to the limb, the calculated distance is 401×10^6km, considerably larger than the asteroid's actual

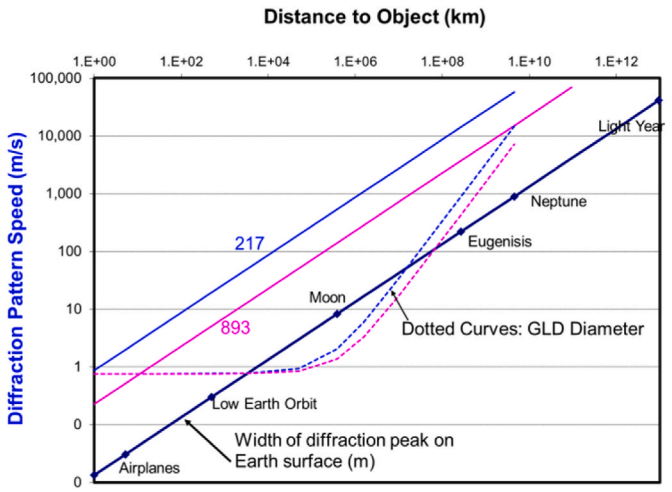

Fig. 23. Diffraction pattern speed vs. distance. Note that HD217014, being closer to Earth than HD89289, has the largest apparent diameter and thus the smallest distance range producing useable diffraction.

distance. This illustrates the importance of measuring the shadow's velocity ***normal*** to the diffracting edge.

If the observed pulses of HD89389 and HD217014 were due to diffraction, the shadow's ground speed could be calculated as a function of distance by dividing the predicted diffraction peak width versus distance by the measured peak duration. Fig. 23 shows these calculated curves, labelled 893 and 217. Also plotted are the GLD curves for both stars. The locations where these curves cross the diffraction curve (solid line) predict the following ranges of possible distance: HD89389: 3,300 to 69,000,000km; HD217014: 3,300 to 16,000,000km. These ranges could be reduced to a single measured value if the speed that the diffraction pattern moved across the ground had been measured.

5.7. Measuring speed using an optical telescope array (OTA)

A single telescope cannot measure the shadow's speed. Fig. 24 suggests that more could be learned if an array of synchronized telescopes is used to observe future events, accurately measuring the time required for the shadow to move between telescopes. Such an array could be readily implemented with modern technology. A good location would be near an existing observatory where good observing conditions (low atmospheric scintillation) have been demonstrated. Smaller telescopes could be used by observing brighter stars. Targets would probably not need to be restricted to solar class, instead concentrating on intrinsically small, bright stars to give the maximum diffraction range. Individual stations could act independently, accurately synchronized using individual GPS PPS signals. Programs similar to those used here could search each telescope's data for signals and record accurate timing for everything that's found. Human interaction would be needed only to confirm the identity of false targets and interpreting the signals when something interesting is found.

Depending on the size of the occulting object relative to array of ground stations, the OTA could also provide important information in addition to the speed and distance of these objects. With an array of sufficient size and density, much could also be learned about the object's size and shape.

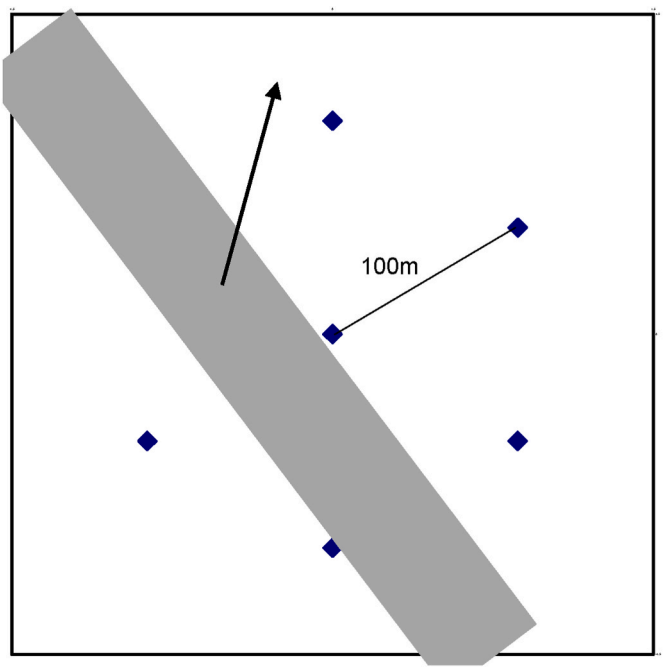

Fig. 24. Array of optical telescopes measuring shadow speed of objects passing in front of bright stars. Note that even if the actual motion is oblique to the diffracting edge (arrow), measured time intervals between telescopes determine its speed normal to this edge, as required in equation (3).

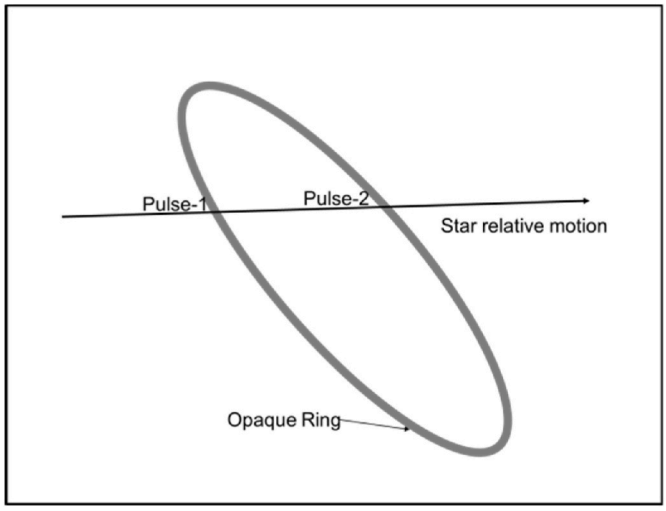

Fig. 25. Possible geometry for producing two pulses.

6. Conclusion

How are two nearly identical pulses generated, separated by a relatively long interval of unaffected starlight? The fact that these pulses have been detected only in pairs must surely be a clue to their origin. How can the two detected events[1] separated by years, and from seemingly random directions in the sky, be so similar to each other? Even if the diffraction theory is correct, these data alone cannot determine the

[1] A third double pulse event has just been found in the light of HD12051 observed on January 18, 2025. The two pulses in this event are separated by 1.52s.

object's distance or velocity. More and better data are needed, such as could be gathered using arrays of telescopes on the ground. Data from this new source, or information from other approaches, may be the only way to unravel this mystery.

One can imagine using a simple model like the structure shown in Fig. 25, to explain the pulses. This thin opaque ring, located somewhere in the solar system, would sequentially occult the star as it moved across the field. If anything like this were found, it would immediately raise the questions of where it came from and how it could survive millions of years of collisions with other objects. Alternatively, if the measured transverse velocity proved greater than that required to escape our solar system, a different set of questions would arise. Whatever is found, those speculating that our best chance of finding evidence of extraterrestrial intelligence lies within our own solar system [15], might have much to ponder!

Declaration of competing interest

The author declares that he has no known competing financial interests or personal relationships that could have appeared to influence the work reported in this paper.

Acknowledgements

The author thanks both anonymous referees for their many helpful comments that significantly improved the manuscript, and also Darle Tilly for her important editorial suggestions.

References

[1] R.H. Stanton, Optical SETI searches: amateur's inside track, in: Proceedings 43th Annual Symposium on Telescope Science, Ontario, CA, 2024, pp. 98–104.
[2] R.H. Stanton, Exploring optical SETI's middle ground, Acta Astronaut. 156 (2019) 92–99.
[3] B. Howard, Optical SETI using a 3-beam coincident photometer, in: Proc. 34th Annual Symposium on Telescope Science, Ontario, CA, 2015, pp. 79–82.
[4] A.W. Howard, P. Horowitz, D.T. Wilkinson, et al., Search for nanosecond optical pulses from nearby solar type stars, ApJ 613 (2004) 1270.
[5] R.N. Schwartz, C.H. Townes, Interstellar and interplanetary communication by optical masers, Nature 190 (1961) 205.
[6] E.F. Borra, Searching for extraterrestrial intelligence signals in astronomical spectra, including existing data, ApJ 144 (2012) 181–187.
[7] N.K. Tellis, G.W. Marcy, A search for optical laser emission using Keck HIRES, PASP 127 (2015) 540–551.
[8] B. Warner, High Speed Astronomical Photometry, Cambridge Univ. Press, 1988.
[9] International Occultation Timing Association (IOTA), https://occultations.org.
[10] R. Nityananda, Diffraction at a straight edge, Resonance (2015) 389–400. https://www.ias.ac.in/article/fulltext/reso/020/05/389-499.
[11] R.Nugent, Ed., Chasing the Shadow—The IOTA occultation observer's manual, www.poyntsource.com/IOTAmanual/IOTA_observers_manual_all_pages.pdf, 381p.
[12] M. Born, E. Wolf, Principles of Optics, Pergamon Press, 1965, pp. 431–435.
[13] R.E. Nather, D.S. Evans, Photoelectric measurements of lunar occultations. I. The process, Astron. J. 75 (1970) 575.
[14] Glorfindel, How to calculate a straight edge diffraction pattern? https://physics.stackexchange.com/questions/2322542020-8-16.
[15] A. Tough, G.A. Lamarchand, Searching for extraterrestrial technologies within our solar system, IAU Symposium 213 (2004) 487–490.